Int. J. Nano Dimens., 11 (1): 41-49, Winter 2020

ORIGINAL ARTICLE

Adsorption and photodegrading of Methylene Blue by using of $BaLa_xGd_xFe_{12-2x}O_{19}$ (x=0.2, 0.4, 0.6 and 0.8)/PANI nanocomposites

Fatemeh Abdollahi [1], Mohammad Yousefi [2,], Malak Hekmati [3], Ana Khajehnezhad [4], Seyyed Salman Seyyed Afghahi [5]*

[1] *Department of Chemistry, Science and Research Branch, Islamic Azad University, Tehran, Iran*

[2] *Department of Chemistry, Yadegar-e Imam Khomeini (RAH) Shahr-e Rey Branch, Islamic Azad University, Tehran, Iran*

[3] *Department of Organic Chemistry, Faculty of Pharmaceutical chemistry, Tehran Medical Sciences, Islamic Azad University, Tehran, Iran*

[4] *Physics Research Center, Science and Research Branch, Islamic Azad University, Tehran, Iran*

[5] *Department of Engineering, Imam Hossein University, Tehran, Iran*

Received 08 August 2019; revised 01 December 2019; accepted 05 December 2019; available online 05 December 2019

Abstract

In this paper, a series of $BaLa_xGd_xFe_{12-2x}O_{19}$ (x=0.2, 0.4, 0.6 and 0.8)/PANI (polyaniline) nanocomposites synthesized for investigating the photocatalytic properties. Barium hexaferrite doped with La^{3+} and Gd^{3+} prepared via a sol-gel auto-combustion method and then the binary nanocomposites fabricated by the in situ polymerization method. (Fourier transform infrared) FTIR, (x-ray diffraction) XRD, (field emission electron microscopy) FESEM and (vibrating sample magnetometer) VSM confirmed the formation of binary nanocomposites. In FTIR analysis, the peaks at 431 and 580 cm^{-1} wavenumbers supported the formation of barium doped hexaferrite. At 1463 and 1554cm^{-1} wavenumbers, the formations of quinoid and benzenoid rings were observable. The XRD patterns of nanocomposites proved the formation of PANI by appearing the amorphous peak at 2θ=23.05 and 26.05 degrees beside the hexaferrite phase. In FESEM pictures, the sphere shape of PANI masked the whole nanoparticles of hexaferrite. In VSM hysteresis loops, by doping La^{3+}, the saturation magnetization increased to 74 emu. Then, by adding non-magnetic part (PANI) to the magnetic hexaferrite, the saturation magnetization decreased to 11 emu. The photocatalytic properties of samples performed under the irradiation of UV-Vis light. All samples presented the photocatalytic properties. Hexaferrites as a semiconductor generated the electron-hole pairs under irradiation. PANI prevented the accumulation of electron-hole pairs on the valance band and consequently accelerated the photo-degradation of methylene blue. Kinetic studies and calculation of the correlation coefficient (R^2) value which was about 0.98, proved that the photocatalytic reactions followed the Pseudo-first order kinetic.

Keywords: *Hexaferrite; Methylene Blue; PANI; Photocatalytic Property; Saturation Magnetization.*

How to cite this article

Abdollahi F, Yousefi M, Hekmati M, Khajehnezhad A, Seyyed Afghahi SS. Adsorption and photodegrading of Methylene Blue by using of $BaLa_xGd_xFe_{12-2x}O_{19}$ (x=0.2, 0.4, 0.6 and 0.8)/PANI nanocomposites. Int. J. Nano Dimens., 2020; 11 (1): 41-49.

INTRODUCTION

M-Type hexaferrites with high resistivity, low density and good chemical stability are utilized in various applications such as: permanent magnets [2], photocatalysts [3] and electromagnetic absorbers[4]. M-Type hexaferrites, with hexagonal structure, consist of R and S blocks. S blocks make from two spinel units with general formula of MFe_2O_4 while R blocks make from three hexagonal layers. Fe^{3+} ions in hexaferrite structures occupy five various positions (octahedrons (2a, 12k and $4f_2$), tetrahedron ($4f_1$), and trigonal bipyramidal (2b) in which $4f_1$ and $4f_2$ are antiparallel and 2a, 12k and 2b are parallel [5]. Due to the different applications of hexaferrites, barium hexaferrites or $BaFe_{12}O_{19}$ were synthesized by various methods

* Corresponding Author Email: myousefi50@hotmail.com

such as sol-gel, co-precipitation, hydrothermal and sol-gel auto-combustion process [6-10]. Among these methods, sol-gel auto-combustion is promising due to the time consuming synthesize method, low cost of the precursors and the easy preparation process [11]. Therefore, barium hexaferrite were synthesized via affordable sol-gel auto-combustion procedure.

Recently, industrial wastewater pollution, due to the organic azo dye contaminants such as methylene blue (MO) can cause hazardous health and environmental problems for humankinds and environments. Respiratory system, eye, nose and skin irritation will appear by contacting with the polluted wastewater. Several methods applied for decomposing and degradation of dye contaminants[12, 13]. Photocatalytic degradation is one of the deceptive methods for removing azo organic dyes by using magnetic semiconductors such as Fe_2O_3, $SrFe_{12}O_{19}$ and $BaFe_{12}O_{19}$ [14, 15]. In the separation process of photocatalysts from wastewater, magnetic semiconductors can easily extract by the external magnetic fields.

Under the light irradiation, the excited electron of valance band can transfer to the conducting band which can create the electron-hole pairs [16]. By adding polyaniline (PANI) as a conductive polymer, with high stability, the process of dye degradation will be enhanced by preventing from the recombination of electron-hole pairs. As a result, binary nanocomposites with the polymer matrix such as PANI/magnetic, polypyrrole/magnetic, PANI/Ba-hexaferrite and polypyrrole hexaferrite have attracted the attention of researcher in the degradation of photocatalytic properties [17].

Because PANI/hexaferrites nanocomposites investigated rarely as a suitable photocatalyst, thus, in this paper, $BaLa_xGd_xFe_{12-2x}O_{19}$ (x=0.2, 0.4, 0.6 and 0.8) were prepared by sol-gel auto-combustion process. Consequently, the binary nanocomposites of $BaLa_xGd_xFe_{12-2x}O_{19}$ (x=0.2, 0.4, 0.6 and 0.8)/ PANI were synthesized by in situ polymerization. Then, FTIR, XRD and FESEM performed for characterization of all samples. The photocatalytic process has carried out to estimate the degradation percentage of all samples. The kinetics, mechanism and the rate of photocatalytic degradation reactions were investigated.

MATERIALS AND METHODS

Nitrate metal salts: $Ba(NO_3)_2$, $Fe(NO_3)_3.9H_2O$, $La(NO_3)_2.6H_2O$, $Gd(NO_3)_2.6H_2O$ used without any excess purification. Citric acid, ammonium peroxydisulfate (APS), distilled aniline twice and hydrochloric acid utilized for synthesis process (all were purchased from Merck Company).

Hexaferrite preparation via sol-gel autocombustion process

Metal oxide salts $Ba(NO_3)_2$, $Fe(NO_3)_3.9H_2O$, $La(NO_3)_2.6H_2O$, $Gd(NO_3)_2.6H_2O$ and citric acid dissolved in deionized water (stoichiometric ratio 2:1) and then the solution heated up to 80˚C. Ammonium hydroxide solution (50% v/v) added to adjust pH to 7. The solution heated up to 110˚C. After two hours, the gel ignited, and a brown powder was gained. The products calcined at 900˚C for 4 hours.

PANI/hexaferrite nanocomposites via in situ-polymerization

3 g of the ammonium peroxydisulfate dissolved in 0.1 M hydrochloric acid (solution A). 1ml of aniline, 0.1g of hexaferrite and 60 ml hydrochloric acid 1M sonicated for 1 hour (solution B). After the sonication process, solution A poured into the solution B drop wise. The polymerization process has been completed in 8 hours at 0-5 ˚C. The samples filtered and dried at 70 ˚C for 24 hours.

Photocatalytic studies

0.2 g of each sample as a photocatalyst added to the 20 ml of methylene blue (MB) solution and stirred for about 1 hour to reach the maximum absorption. Then, the samples irradiated under the Hg-UV lamp (400). For preventing the temperature increasing, the whole system placed in the container in which the water circulated, consequently, the temperature remains at 25 ˚C. On the certain interval times, the samples taken out and then filtered and washed with deionized water. Then, the products were investigated by UV spectrophotometer.

Characterization

The FTIR analysis of samples for asserting functional group was studied by Bruker- Tensor27 apparatus. Philips Xpert diffractometer by CuK_α radiation at 2θ= 20-80 with 0.05° was utilized for XRD characterization. FESEM micrograph of samples was performed by SIGMA VP-500, the ZEISS model. VSM hysteresis loops were studied by ZVK, R&S. Photocatalytic studies was investigated by UV- Visible spectrometer CARY, 300 Conc.

RESULTS AND DISCUSSIONS

FTIR analysis

FTIR spectrums presented at Fig. 1(a-d). In the structure of hexaferrites, the two main peaks at 431and 580cm^{-1} corresponded to the vibration of the Fe-O bond at tetrahedral and octahedral structure. Because of the short length of the tetrahedral structure rather than octahedral structure, the vibrational modes of tetrahedral are appeared at the higher wavenumber[18].

In the binary nanocomposites, by increasing the dopants, the peaks at 580cm^{-1} wavenumber shifted to the higher wavenumbers because of the forces between nanocomposites [19]. The formation of quinoid and benzenoid rings of PANI was observed at 1463 and 1554cm^{-1} wavenumbers which related to the stretching bond of C=C. The peaks at 1238 and 1290 cm^{-1} regarding to the N-H bending and asymmetric C-H stretching bands of benzenoid rings. The vibration of N=Q=N in the quinoid ring observed at 1105cm^{-1} wavenumber. For the polyaniline the peak observed at 1456 cm^{-1} can be related to C=C and C=N stretching mode of benzenoid unite [20, 21].

For more comparison between the observed absorption bands, the vibrational assignments for PANI and hexaferrites were listed in a Table 1.

XRD patterns

The XRD patterns of $BaLa_xGd_xFe_{12-2x}O_{19}$ (x=0.2, 0.4, 0.6 and 0.8)/PANI show at Fig. 2 (a-d). The peaks of barium hexaferrites at 2θ: 30.65, 32.25, 34.55, 37.25, 40.7, 55.15 and 56.5 degree confirm the formation of hexaferrites phase which is

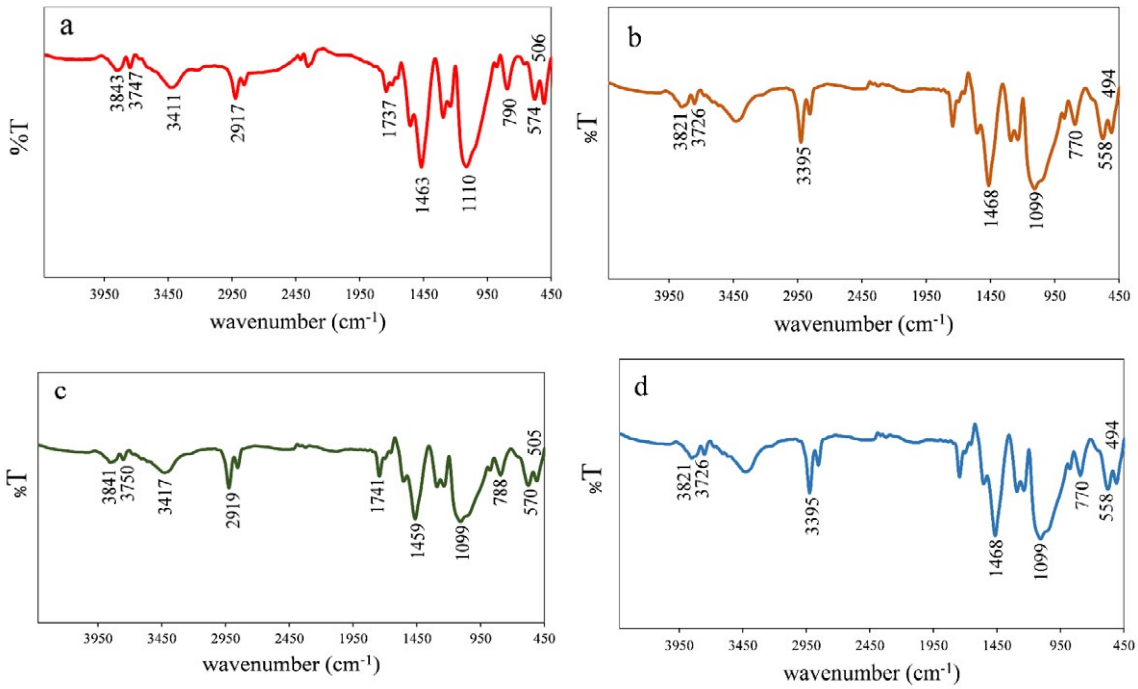

Fig. 1. FTIR $BaLa_xGd_xFe_{12-2x}O_{19}$ a) x=0.2, b) 0.4, c) 0.6 and d) 0.8)/PANI.

Table 1. The vibrational assignments for PANI and hexaferrites.

Samples	Mechanism	R^2 values	Decolorization efficiency %
$SrFe_{12}O_{19}$	First-order	0.94	92%
Cobalt ferrite–polyaniline	Second-order	0.99	98%
$BaFe_{12}O_{19}$	-	-	70%
Zinc-doped cobalt ferrite	First-order	098	-
CNTs/P-TiO2	pseudo-first-order	-	-
PANI_BiOCl	pseudo-first-order		67%

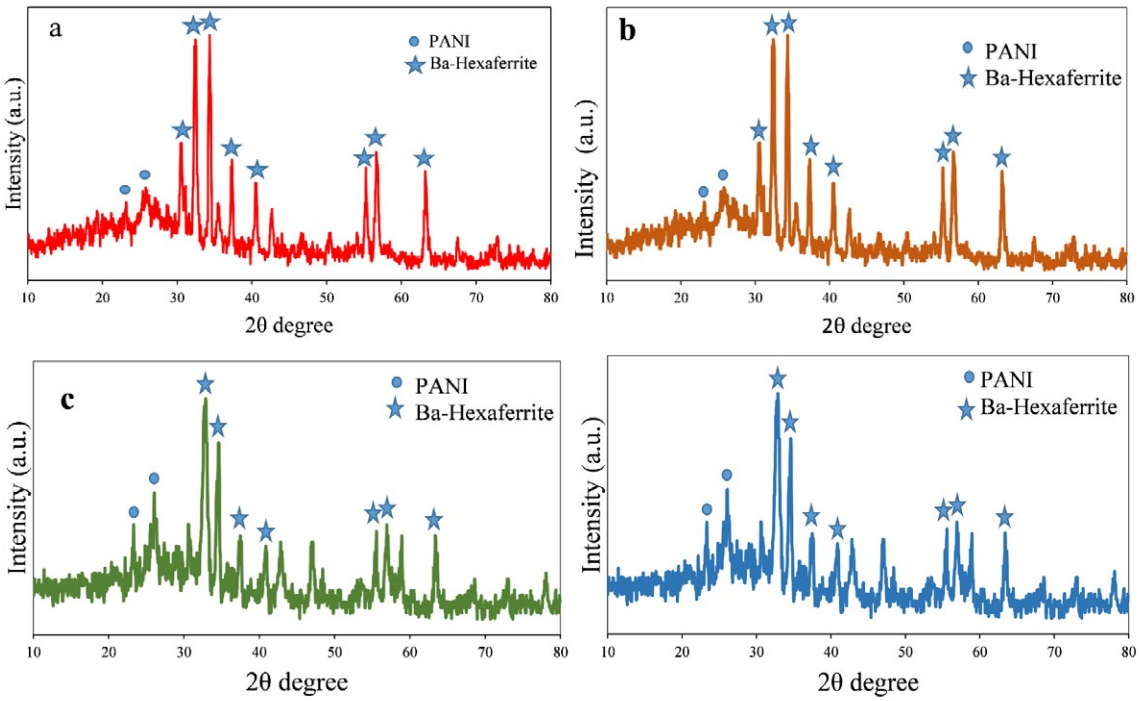

Fig. 2. XRD $BaLa_xGd_xFe_{12-2x}O_{19}$ a) x=0.2, b) 0.4, c) 0.6 and d) 0.8)/PANI.

matched with JCPDS 027-1029 [22]. No impurities were observed in the XRD patterns of samples. In the binary nanocomposites, the broad peak at 2θ=23.05 and 26.05 degree have revealed the PANI formation. By increasing the dopants, small shift to the small angles appeared due to the difference between lattice parameters [23].

The cell volume and the lattice parameters were calculated from the equations (1):

$$\frac{1}{d^2}=\frac{4}{3}\left(\frac{h^2+hk+k^2}{a^2}\right)+\frac{l^2}{c^2} \quad (1)$$

Where d is the crystal plane distance, *a, and c* are lattice parameters, *h*, *k* and *l* are Miller indices. Regarding to the larger radius of La^{3+} (1.22Å) and Gd^{3+} (1.07Å) in comparison to the Fe^{3+} (0.63Å), the crystallite size of $BaLa_xGd_xFe_{12-2x}O_{19}$ (x=0.2, 0.4, 0.6 and 0.8) increased by increasing dopants substitution (84, 103, 128, and 134 nm).

FESEM micrograph

FESEM micrograph of $BaLa_xGd_xFe_{12-2x}O_{19}$ (x=0.2, 0.4, 0.6 and 0.8)/PANI represented at Fig. 3(a-d). In all samples the agglomeration of particles due to the magnetic properties of hexaferrite was observable. The sphere shape of PANI covered the whole surface of hexagonal barium hexaferrite. Consequently particles of the polymer masked the whole hexaferrites, so the sphere shape of PANI was observable [24].

The average size of agglomeration for $BaLa_xGd_xFe_{12-2x}O_{19}$ (x=0.2, 0.4, 0.6 and 0.8)/PANI were 92, 123, 148, and 169 nm which represented that the agglomeration cause the increasing of the average particles size.

VSM hysteresis loops

VSM hysteresis of samples depicted at Fig. 4. Saturation magnetization of pure barium hexaferrites is about 60 emu while the coercivity is about 5000 Oe. Fe^{3+} ion in the structure of hexaferrites occupied the octahedral (12k, $4f_2$ and 2a) sites, tetrahedral ($4f_1$) site and trigonal (2b) site with three spin- up (2a, 2b, 12k) positions and two spin- down ($4f_1$, $4f_2$) positions [25]. The results ascribe that La^{3+} occupies $4f_2$ down spin site which increases the number of Fe^{3+} at spin up sites more than spin down positions [1], and consequently enhances the saturation magnetization to 74 emu. By adding PANI as a non-magnetic polymer, the saturation magnetization decreased abruptly. As a result by adding non-magnetic part (PANI) to the magnetic hexaferrite,

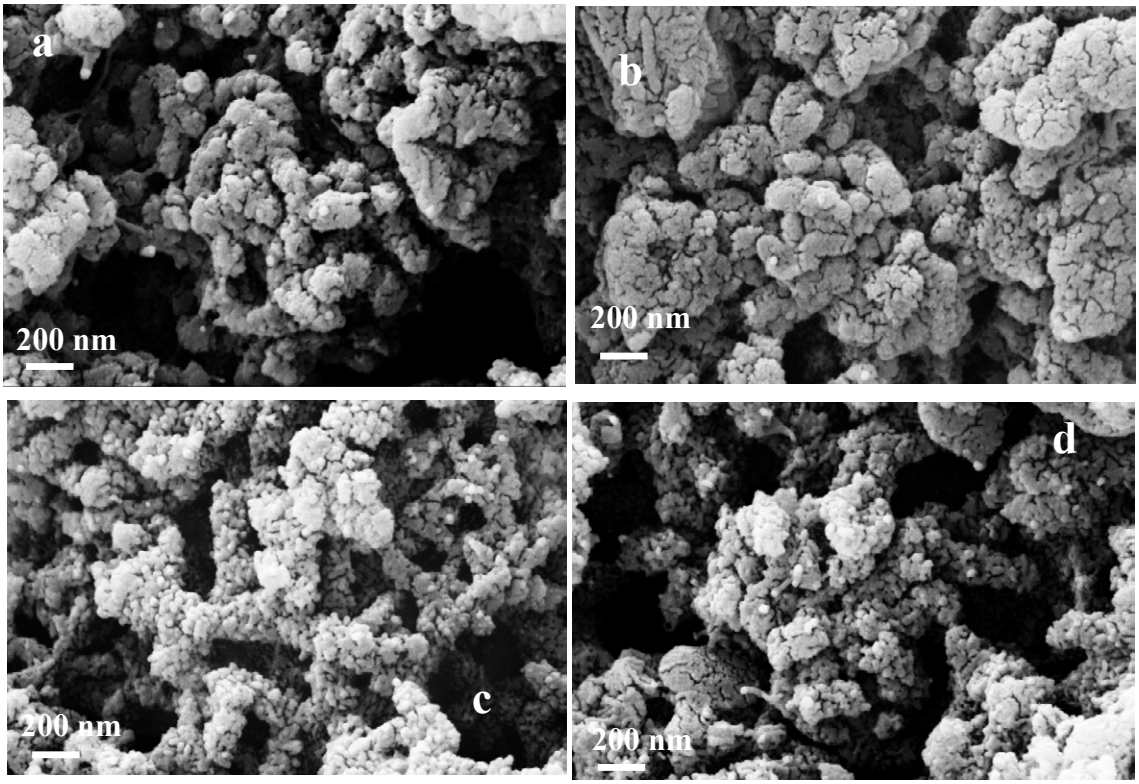

Fig. 3. FESEM of $BaLa_xGd_xFe_{12-2x}O_{19}$/PANI a) x=0.2, b) 0.4, c) 0.6 and d) 0.8.

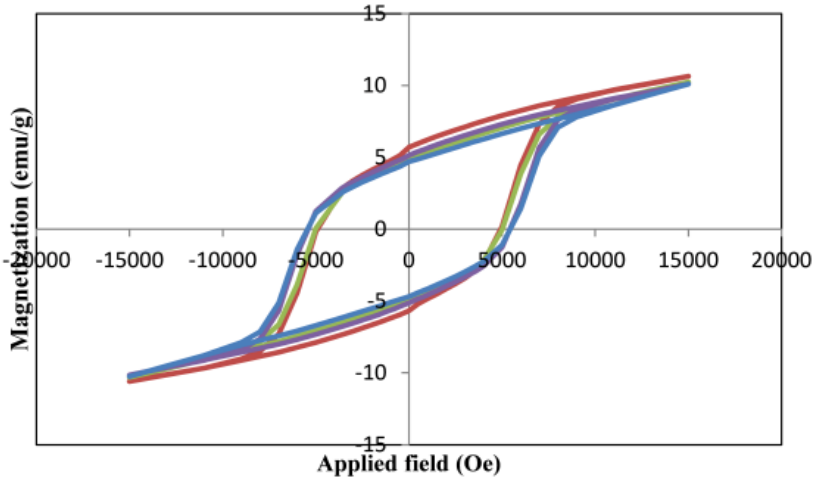

Fig. 4. VSM hysteresis loops of $BaLa_xGd_xFe_{12-2x}O_{19}$/PANI x=0.2, 0.4, 0.6 and 0.8.

the saturation magnetization dropped remarkably (60 to 11 emu).

The magnetic data were listed at Table 2.

Kinetic studies

The kinetic of the photocatalytic process of all samples monitored (Fig. 5 (a-d)). The kinetic results show that the photocatalytic reactions followed the Pseudo-first order kinetic model. In the Pseudo-first order kinetic model, one of the reactant acts as the catalyst and the concentration of this reactant keeps unchanged during the reaction. By increasing the substrate concentration [A], the catalyst surface covers completely the

Table 2. The magnetic data of $BaLa_xGd_xFe_{12-2x}O_{19}$/PANI x=0.2, 0.4, 0.6 and 0.8.

Samples	Wavenumbers (cm^{-1})	Vibrational modes
$BaLa_xGd_xFe_{12-2x}O_{19}$ (x=0.2, 0.4, 0.6 and 0.8)/PANI	431 and 580	Fe-O tetrahedral and octahedral structure
	1463 and 1554	quinoid and benzenoid rings of PANI
	1238and 1290	N-H bending and asymmetric C-H stretching bands of benzenoid rings
	1105	N=Q=N quinoid ring
	1456	C=C and C=N stretching of benzenoid

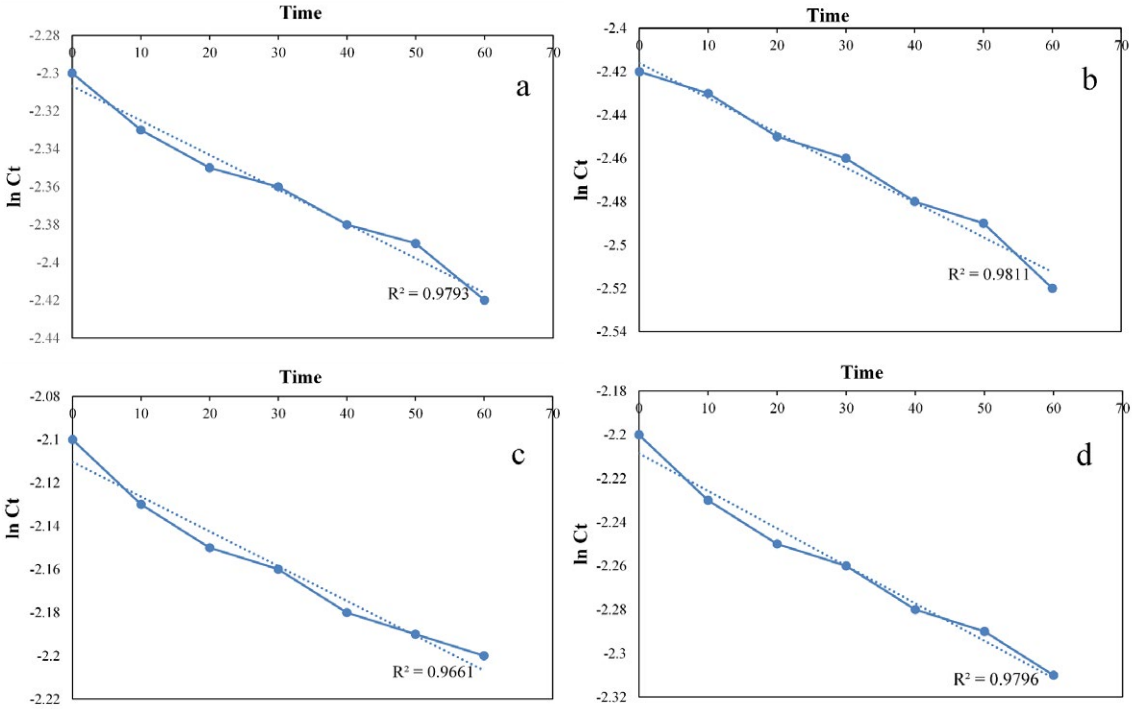

Fig. 5. Kinetic of the photocatalytic process of $BaLa_xGd_xFe_{12-2x}O_{19}$/PANI a) x=0.2, b) 0.4, c) 0.6 and d) 0.8.

substrate and consequently the reaction becomes dependent on the substrate concentration. In this situation the whole reaction is in accordance with the following equation:

$Ln[A]_t-ln[A]_0=-k't$

$Ln[A]_t=ln[A]_0- k't$

A curve of ln $[A]_t$ versus t should give a straight line which the slope is - k. The intercept of the plot is ln $[A]_0$ [26].{Mittal, 2010 #5}

The correlation coefficient (R^2) value (for $BaLa_xGd_xFe_{12-2x}O_{19}$ (x=0.2, 0.4, 0.6 and 0.8)/PANI, the coefficient values (R^2) are about 0.97, 0.98, 0.96, and 0.97) confirms that the photocatalytic reactions in this work followed the Pseudo-first order kinetic.

The decolorization efficiency percentage was calculated from the following equation:

$$\frac{C_{0-C}}{C_0}\times 100 = \text{Decolorization efficiency percentage (\%)}$$

in which C_0 is the initial concentration, and C is the concentration of MB in aqueous solution after equilibrium. In this study the decolorization efficiency percentage for $BaLa_xGd_xFe_{12-2x}O_{19}$ (x=0.2, 0.4, 0.6 and 0.8)/PANI are 86, 92, 79, and 87%. According to the decolorization efficiency

Table 3. The comparison of reported adsorbents.

samples	M_s(emu/g)	M_r	H_c(Oe)
X=0.2/PANI	10.41	5.67	5000
X=0.4/PANI	10.05	5.6	5100
X=0.6/PANI	8.5	6.7	5008
X=0.8/PANI	9.97	4.7	5200

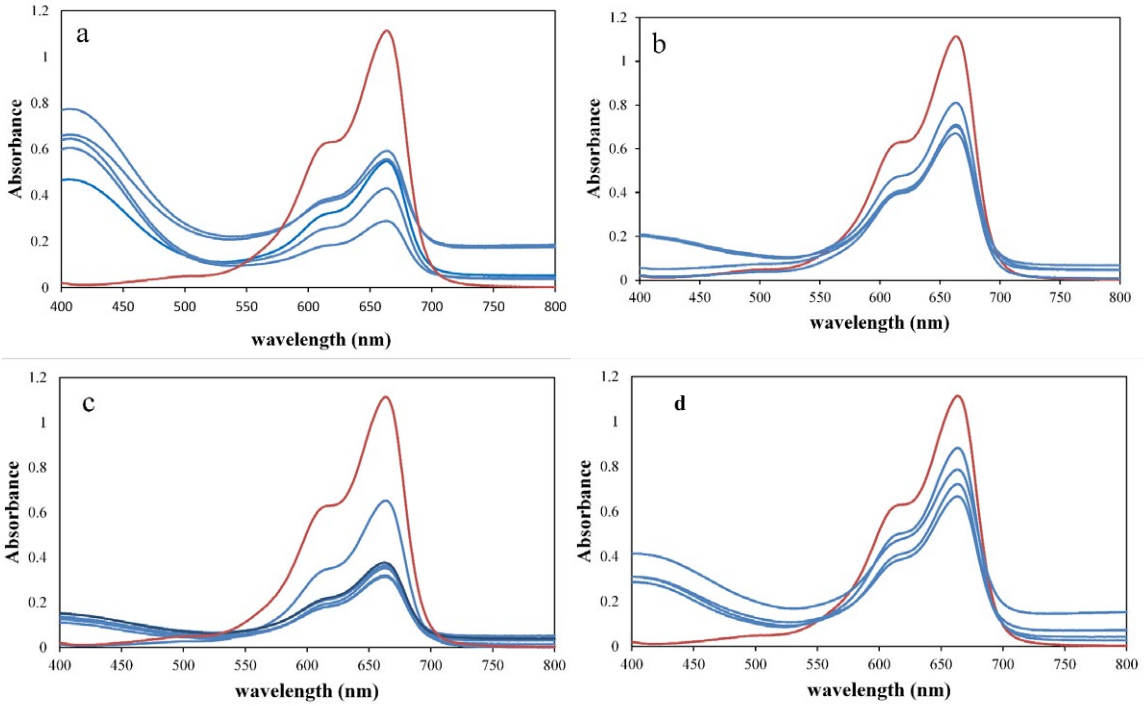

Fig. 6. The absorbance versus wavelength curves of $BaLa_xGd_xFe_{12-2x}O_{19}$/PANI a) x=0.2, b) 0.4, c) 0.6 and d) 0.8.

percentage, $BaLa_xGd_xFe_{12-2x}O_{19}$ (x=0.2, 0.4, 0.6 and 0.8)/PANI nanocomposite show better photocatalytic activity rather than other samples. For comparing prepared samples with other adsorbents, the photocatalytic activities and kinetic studies of some adsorbents were listed at Table 3.

Photocatalytic Properties

The photocatalytic properties of samples presented at Fig. 6 (a-d). The absorbance versus wavelength curves reveals that all samples are photocatalyst.

Under visible light irradiation, hexaferrite nanoparticles were excited and the electron-hole (e^-/h^+) pairs in conducting and valance band fabricated. The holes reacted with H_2O molecules and OH^- radicals was generated [27]. The free radicals interacted with methylene blue dyes and degrade it.

$BaFe_{12}O_{19}+hv \rightarrow (e^-) + (h^+)$

$(e^-) + O_2 \rightarrow {}^{\cdot}O_2^-$

$(h^+) + H_2O \rightarrow OH^{\cdot}$

$OH^{\cdot}+MB \rightarrow CO_2 + H_2O +$ nontoxic products

${}^{\cdot}O_2^- + e^- + 2H^+ \rightarrow H_2O_2$

$H_2O_2 \rightarrow 2OH^-$

${}^{\cdot}O_2^- + MB \rightarrow CO_2 + H_2O +$ nontoxic products

π to π^* transitions of PANI took place under visible light irradiation in binary nanocomposite. Consequently, the holes of valence band could easily transfer to the π orbital of PANI and the electrons transfer to π^* orbital. As a result, the charge carriers simply migrated to the surface of nanocomposite and degrade the methylene blue dye [28-34]. PANI prevented the accumulation of electron-hole pairs on the valance band and consequently accelerated the photo-degradation of methylene blue.

CONCLUSION

$BaLa_xGd_xFe_{12-2x}O_{19}$ (x=0.2, 0.4, 0.6 and 0.8)/PANI nanocomposites were synthesized successfully via in situ polymerization. The peaks at 431and 580cm^{-1} wavenumber represent the formation of Fe-O bond at tetrahedral and octahedral structure. By increasing dopants, the peaks at 580cm^{-1} bond shifted to the higher frequency because of the forces between nanocomposites. In XRD patterns, the broad peak at 2θ=23.05 and 26.05 degree confirm the PANI

formation. By adding PANI as a non-magnetic polymer, the saturation magnetization decreased suddenly. After monitoring the photocatalytic properties of samples, the photocatalytic results and curves reveal that all samples represent the photocatalytic properties and can degrade the MB dye. The kinetic studies of samples represent that the photocatalytic reactions followed the Pseudo-first order kinetic model.

DISCLOSURE STATEMENT

All authors declare that they have no conflict of interest in the publication of this manuscript.

REFERENCES

[1] Kang Y.-M., (2015), High saturation magnetization in La–Ce–Zn–doped M-type Sr-hexaferrites. *Ceram. Int.* 41: 4354-4359.

[2] Meng P., Xiong K., Wang L., Li S., Cheng Y., Xu G., (2015), Tunable complex permeability and enhanced microwave absorption properties of BaNixCo1−xTiFe10O19. *J. Alloys Comp.* 628: 75-80.

[3] Roshanaei K., (2016), Controlled synthesis and photocatalytic activities of barium hexaferrite nanoparticles and examine decolorization methyl orange on liver of rats. *J. Mater. Sci: Mater. Electron.* 28: 4537-4544.

[4] Velhal N., Kulkarni G., Mahadik D., Chowdhury P., Barshilia H., Puri V., (2016), Effect of Ba^{+2} ion on structural, magnetic and microwave properties of screen print ed BaxSr1-XFe12O19 thick films. *J. Alloys Comp.* 682: 730-737.

[5] Pullar R. C., (2012), Hexagonal ferrites: A review of the synthesis, properties and applications of hexaferrite ceramics. *Prog. Mater. Sci.* 57: 1191-1334.

[6] Davoodi A., Hashemi B., (2011), Magnetic properties of Sn–Mg substituted strontium hexaferrite nanoparticles synthesized via coprecipitation method. *J. Alloys Comp.* 509: 5893-5896.

[7] Afghahi S. S. S., Jafarian M., Atassi Y., (2016), Microstructural and magnetic studies on BaMgxZnxX2xFe12−4xO19 (X=Zr, Ce, Sn) prepared via mechanical activation method to act as a microwave absorber in X-band. *J. Magnet. Magnetic Mater.* 406: 184-191.

[8] Durmus Z., Kavas H., Durmus A., Aktaş B.,(2015), Synthesis and micro-structural characterization of graphene/ strontium hexaferrite (SrFe 12 O 19) nanocomposites. *Mater. Chem. Phys.* 163: 439-445.

[9] Hongfei L., Jian jiang W., Baocai X., Guoshun W., Yongshen H., Haitao G., Weimin Y., (2015), Effects of Mg or Sr doping on the intrinsic characteristics and absorption properties of micro-nano BaFe12O19 hollow multiphase ceramic microspheres. *J.Mag. Magnet. Mater.* 374: 530-538.

[10] Sözeri H., Mehmedi Z., Kavas H., Baykal A., (2015), Magnetic and microwave properties of BaFe12O19 substituted with magnetic, non-magnetic and dielectric ions. *Ceram. Int.* 41: 9602-9609.

[11] Ghezelbash S., Yousefi M., Hossainisadr M., Baghshahi S., (2018), Structural and magnetic properties of Sn^{4+} doped strontium hexaferrites prepared via sol–gel auto-combustion method. *IEEE Transact. Magnet.* 54: 1-6.

[12] Ammar Houasa H. L., Ksibia M., Elaloui E., Chantal Guillard J.-M. H., (2001), Photocatalytic degradation pathway of methylene blue in water. *Appl. Catal. B: Env.* 31: 145–157.

[13] Mikhaylov S., Pud A., Wojkiewicz J.-L., Coddeville P., (2017), UV-light induced solid-phase photodegradation in PANI nanocomposites. *Nanomaterials: Application & Properties (NAP), 2017 IEEE 7th International Conf.* 2017: IEEE, pp. 03NNSA09-1-03NNSA09-4.

[14] Ebrahimi Z., Hedayati K., Ghanbari D., (2017), Preparation of hard magnetic BaFe12O19–TiO2 nanocomposites: applicable for photo-degradation of toxic pollutants. *J. Mater. Sci: Mater. Electronic.* 28: 13956-13969.

[15] Hong X., Xie Y., Wang X., Li M., Le Z., (2015), A novel ternary hybrid electromagnetic wave-absorbing composite based on BaFe 11.92 (LaNd)0.04O19-titanium dioxide/ multiwalled carbon nanotubes/polythiophene. *Compos. Sci. Technol.* 117: 215-224.

[16] Mishra D. D., Huang Y., Duan N., Tan G., (2018), Visible photocatalytic degradation of methylene blue on magnetic semiconducting La0.2Sr0.7Fe12O19. *J. Mater. Sci: Mater. Electron.* 29: 9854-9860.

[17] Xiong P., Chen Q., He M., Sun X., Wang X., (2012), Cobalt ferrite–polyaniline heteroarchitecture: a magnetically recyclable photocatalyst with highly enhanced performances. *J. Mater. Chem.* 22: 17485-17489.

[18] Mousavinia M., (2014), Structural, magnetic, and reflection loss characteristics of Ni/Co/Sn-substituted strontium ferrite/functionalized MWCNT nanocomposites. *J. Electron. Mater.*43: 2573-2583.

[19] Afghahi S. S. S., Peymanfar R., Javanshir Sh., Atassi Yomen., Jafarian M., (2016), Synthesis, characterization and microwave characteristics of ternary nanocomposite of MWCNTs/doped Sr-hexaferrite/PANI. *J. Magnet. Mag. Mater.*423: 152-157.

[20] Li Y., (2012), Preparation, magnetic and electromagnetic properties of polyaniline/strontium ferrite/multiwalled carbon nanotubes composite. *Appl. Surf. Sci.*258: 3659-3666.

[21] Gairola S. P., Verma V., Kumar L., Abdullah Dar M., Annapoorni S., Kotnala R. K., (2010), Enhanced microwave absorption properties in polyaniline and nano-ferrite composite in X-band. *Synth. Metals*. 160: 2315-2318.

[22] Rostami M., (2016), Characterization of magnetic and microwave absorption properties of multi-walled carbon nanotubes/Mn-Cu-Zr substituted strontium hexaferrite nanocomposites. *Mater. Res. Bullet.* 83: 379-386.

[23] Yang C. C., (2011), Synthesis, infrared and microwave absorbing properties of $(BaFe_{12}O19+BaTiO_3)$/polyaniline composite. *J. Magnet. Mag. Mater.*323: 933-938.

[24] Hou J., Cao R., Jiao S., Zhu H., Kumar R. V., (2011), PANI/ $Bi_{12}TiO_{20}$ complex architectures: Controllable synthesis and enhanced visible-light photocatalytic activities. *Appl. Catal. B: Env.* 104: 399-406.

[25] Rai B. K., Mishra S. R., Nguyen N. N., Liu J. P., (2013), Synthesis and characterization of high coercivity rare-earth ion doped Sr0.9RE0.1Fe10Al2O19 (RE: Y, La, Ce, Pr, Nd, Sm, and Gd). *J. Alloys Comp.* 550: 198-203.

[26] Mahdiani M., Sobhani A., Salavati-Niasari M., (2017), Enhancement of magnetic, electrochemical and photocatalytic properties of lead hexaferrites with coating graphene and CNT: Sol-gel auto-combustion synthesis by valine. *Sep. Purif. Technol.* 185: 140-148.

[27] Fu W., (2006), Preparation and photocatalytic

characteristics of core-shell structure TiO_2/$BaFe_{12}O_{19}$ nanoparticles. *Mater. Lett.* 60: 2723-2727.

[28] Valero-Luna C., Palomares-Sanchéz S., Ruiz F., (2016), Catalytic activity of the barium hexaferrite with H_2O_2/ visible light irradiation for degradation of Methylene Blue. *Catal. Today*. 266: 110-119.

[29] Mittal A., (2010), Removal and recovery of chrysoidine Y from aqueous solutions by waste materials. *J. Coll. Interf. Sci.* 344: 497–507.

[30] Gupta V., Jian R., Shirivasta M., (2011), Removal of the hazardous dye—Tartrazine by photodegradation on titanium dioxide surface. *Mater. Sci. Eng. C.* 31: 1062–1067.

[31] Saleh T., Gupta V., (2012), Photo-catalyzed degradation of hazardous dye methyl orange by use of a composite catalyst consisting of multi-walled carbon nanotubes and titanium dioxide. *Coll. Interf. Sci.* 371: 101–106.

[32] Khani H., Rofoui M., Arab P., Gupta V., Vafaei Z., (2010), Multi-walled carbon nanotubes-ionic liquid-carbon paste electrode as a super selectivity sensor: Application to potentiometric monitoring of mercury ion (II). *Hazard. Mater.* 183: 402–409.

[33] Sarvanan R., (2016), Conducting PANI stimulated ZnO system for visible light photocatalytic degradation of colored dyes. *Molec. Liq.* 221: 1029-1033.

[34] Divaraj M., (2016), Preparation of novel shape Cu and Cu/Cu_2O nanoparticles for the determination of dopamine and paracetamol. *Molec. Liq.* 221: 930-941.